The Meteoritical Society

Meteoritics & Planetary Science 51, Nr 6, 1082–1095 (2016)
doi: 10.1111/maps.12646

The oxidation state of nanophase Fe particles in lunar soil: Implications for space weathering

Michelle S. THOMPSON*, Thomas J. ZEGA, Patricio BECERRA, James T. KEANE, and Shane BYRNE

Lunar and Planetary Laboratory, University of Arizona, 1629 E. University Blvd, Tucson, Arizona 85721, USA
*Corresponding author. E-mail: mst@lpl.arizona.edu

(Received 27 April 2015; revision accepted 03 March 2016)

Abstract–We report measurements of the oxidation state of Fe nanoparticles within lunar soils that experienced varied degrees of space weathering. We measured >100 particles from immature, submature, and mature lunar samples using electron energy-loss spectroscopy (EELS) coupled to an aberration-corrected transmission electron microscope. The EELS measurements show that the nanoparticles are composed of a mixture of Fe^0, Fe^{2+}, and Fe^{3+} oxidation states, and exhibit a trend of increasing oxidation state with higher maturity. We hypothesize that the oxidation is driven by the diffusion of O atoms to the surface of the Fe nanoparticles from the oxygen-rich matrix that surrounds them. The oxidation state of Fe in the nanoparticles has an effect on modeled reflectance properties of lunar soil. These results are relevant to remote sensing data for the Moon and to the remote determination of relative soil maturities for various regions of the lunar surface.

INTRODUCTION

Grains on the surfaces of airless bodies such as the Moon and asteroids are continually modified by micrometeorite impacts and interactions with solar-wind ions, processes that are collectively known as space weathering. This phenomenon alters the optical properties of surface soils by darkening and reddening their reflectance spectra and by attenuating their characteristic absorption bands (Hapke 2001). Understanding the changes to optical properties of surface samples on airless bodies is important because these processes have historically made it difficult to match meteorites to their parent asteroids, e.g., ordinary chondrites and S-type asteroids.

Changes in the optical properties of soils have been attributed to the production of iron nanoparticles in surface grains, often referred to as nanophase Fe (npFe), by space weathering processes. These iron nanoparticles occur as inclusions in agglutinitic lunar glasses formed by micrometeorite impact events, and as inclusions in amorphous rims on grains produced by vapor deposition and irradiation processes. The iron nanoparticles range in size from a few to several tens of nm; those in vapor-deposited and irradiation-produced surface rims typically average 3 nm in size in a mature lunar soil whereas those in grain interiors associated primarily with agglutinates are larger, averaging 7 nm in the same mature lunar soil. The size and distribution of these grains has important implications for the optical properties of lunar surface soils (Keller and Clemett 2001). Analysis of lunar soils and experimentally created analogs show that nanoparticles <5 nm increase reflectance with increasing wavelength (redden), whereas particles >10 nm lower the overall reflectance (darken) spectra of surface materials (Keller et al. 1998; Noble et al. 2007).

The nanoparticles in lunar soil samples are typically reported as containing Fe in the reduced metallic state, i.e., Fe^0, and are widely identified as $npFe^0$ in the literature, e.g., Pieters et al. (2000). This hypothesis is based on the reducing nature of the environment in which npFe particles form, and the measured ferromagnetic resonance properties of lunar soils (Morris 1978). However, Keller and Clemett (2001) analyzed lunar agglutinitic glasses containing nanoparticles and showed that the Fe in these samples occurs as both Fe^0 and Fe^{2+} oxidation states. Their

© The Meteoritical Society, 2016.

results suggest that a component of these samples, either the agglutinitic glasses, the nanoparticle inclusions, or both, are composed of mixed-valence Fe. However, direct measurement of the oxidation state of Fe in those nanoparticles was difficult at the time due to spatial and spectral limitations on nearly all available transmission electron microscopes (TEMs).

The presence of mixed-valence Fe has important implications for understanding the effect of npFe on the optical properties of surface samples and on airless body landscape evolution. The refractive properties of Fe vary with oxidation state, affecting the overall reflective properties of the soil in which they occur (Johnson and Christy 1974; Henning et al. 1995). Experimental simulation of micrometeorite impacts and solar-wind exposure using laser and ion irradiation have both formed npFe (Sasaki et al. 2001; Loeffler et al. 2009). Thus, measurement of the oxidation state of individual Fe nanoparticles could help in constraining the nature of these formation mechanisms and the subsequent alteration of these features. Further, such measurements could provide insight into the nature of space-weathering processes on other airless bodies including near-Earth asteroids such as (25143) Itokawa, the target of the Hayabusa mission.

Over the past 10 yr, there have been dramatic improvements in electron optics. Development and implementation of spherical-aberration (C_s) correctors and monochromators in TEMs has pushed spatial resolution into the sub-Ångstrom scale and spectral resolution into the millivolt regime. Direct atomic-resolution imaging and spectroscopy has been realized and these techniques have been applied to electronic and other technologically relevant materials (e.g., Muller et al. 2008; Varela et al. 2009; Krivanek et al. 2010). The application of such methods to Earth and planetary materials has the potential to provide new insights into our origins at a fundamental atomic level. Here, we apply electron energy-loss spectroscopy (EELS) coupled to a C_s-corrected and monochromated TEM to evaluate the oxidation state of individual Fe nanoparticles in lunar soil. We show that Fe occurs in mixed oxidation states and, combining these results with spectral modeling, that these states affect the optical properties of the grains on airless body surfaces.

SAMPLES AND METHODS

We embedded <1 mm grains of three Apollo lunar soils in low-viscosity epoxy and prepared samples for TEM analysis through ultramicrotomy. This preparation technique has previously been used without any adverse effect on the oxidation state of Fe nanoparticles, e.g., Keller and Clemett (2001). The studied samples include: 79221, a mature mare soil; 15071, a submature mare soil; and 12033, an immature mare soil. These samples were chosen because they have similar bulk compositions, but have experienced a range of space weathering, classified from immature to mature. We collected images of our lunar soil samples using the 200 keV JEOL 2500SE analytical scanning TEM (S/TEM) at NASA Johnson Space Center equipped with bright-field (BF) and dark-field (DF) STEM detectors.

To measure the oxidation state of Fe in these nanoparticles we employed core-loss EELS coupled to a TEM. Over 100 individual nanoparticles were measured across all three samples, with over 30 from each sample occurring in several separate lunar soil grains. We analyzed nanoparticles that occur both in vapor-deposited rims around grains and in the interiors of glassy agglutinate grains.

All EELS analyses were performed using the 100 keV monochromated and C_s-corrected Nion UltraSTEM at Arizona State University (ASU), equipped with a Gatan Enfinium spectrometer. Operating conditions included a convergence semiangle of 30 mrad, a 0.2 nm probe size, 3 mm spectrometer entrance aperture, and a collection angle of 45 mrad. We collected EELS spectra with the monochromator on, which provided an energy resolution between 200 and 300 meV as measured from the full-width half-maximum height of the zero-loss peak (ZLP). Individual nanoparticles were measured via line profiles using a 0.1 eV/channel dispersion and a variable dwell time, ranging from 0.01 s px^{-1} to 0.5 s px^{-1}, and a probe current of 0.5 nA. The energy dispersions for the spectrometer were calibrated during each analysis session by measuring the shift of the ZLP with automated routines in the DigitalMicrograph software package used to acquire EELS data.

To assess the effect of sample thickness on spatial resolution of the STEM probe, we calculated the amount of beam broadening that a 0.2 nm probe would experience in the sample. Using equation 36.1 from Williams and Carter (1996):

$$b = 8 \times 10^{-12} \frac{z}{E_o} (N_v)^{1/2} t^{3/2} \quad (1)$$

where b is the beam broadening (m), Z is the average atomic number of the sample, E_o is the beam energy (keV), N_v is the number density of atoms (atoms/m^3), and t is the thickness of the sample (m). We calculated a beam broadening parameter, b, to be 3.82 nm, based on a 100 keV accelerating voltage, an average atomic number of 11.4, assuming clinopyroxene, which composes a significant proportion of the mineral

fragments in mare soils, a sample thickness of 60 nm (the ultramicrotome slice thickness), and N_v *of* 8.2×10^{28} atoms m^{-3} (based on clinopyroxene cell parameters). To find the realized beam size after broadening effects, we used equation 36.2 from Williams and Carter (1996):

$$R = (b^2 + d^2)^{1/2} \quad (2)$$

where R is the realized beam diameter (m), b is the beam broadening parameter described above (m), and d is the incident beam diameter (m). Using the calculated broadening parameter and our incident beam diameter of 0.2 nm, the realized beam diameter is 3.84 nm. This beam diameter is small enough to measure accurately the microstructural features we describe throughout the manuscript.

Spectral processing involved multiple steps. We removed the background from each spectrum, in the form of AE^{-r}, and deconvolved the ZLP using the Fourier-Ratio method (Egerton 1996). We note that the diameter of most particles is <10 nm. As such, the three-dimensional size, assuming the particles are spheres, is less than the overall thickness of the ultramicrotomed thin section (≥60 nm). Thus, EELS spectra obtained from the nanoparticles include a contribution from the surrounding glassy material lying above and/or below the nanoparticle in cross section. This surrounding matrix material can contain a mixture of Fe oxidation states in proportions unequal to that of the nanoparticle itself (Keller and Clemett 2001). In order to account for this effect and isolate the contributions to the collected spectra solely from the nanoparticle, we collected line profiles that transect both the nanoparticle and the matrix material surrounding it. After performing background and ZLP corrections for both the matrix and nanoparticle spectra, we subtracted the average matrix component from the average nanoparticle spectrum, leaving a residual spectrum that is representative of the nanoparticle without matrix effects. From this residual spectrum, we subtracted the continuum intensity beneath the Fe $L_{2,3}$ edge on all spectra using a linear fit between 702 and 725 eV. We note that the continuum intensity has been successfully modeled based on linear and step-function (arctan) fits between edge onset and postedge energies (Garvie and Buseck 1998; van Aken et al. 1998).

We determined the Fe oxidation state of nanoparticles by performing a flux-weighted, linear, least-squares fit between the observed EELS spectra and the spectra of three Fe oxidation endmembers: Fe^0 (Fe metal; 99.98% purity), Fe^{2+} (FeO, wüstite; 99.9% purity), and Fe^{3+} (Fe_2O_3, hematite; 99.9% purity). The wüstite and hematite standards were embedded in epoxy and prepared for the TEM using ultramicrotomy, whereas the Fe metal sample was prepared via focused ion beam (FIB) using the FEI Nova 200 NanoLab FIB at ASU. The standards were measured using the same operating conditions as described above, in order to model quantitatively the measured spectrum from the nanoparticle. The Fe-oxidation-state ratios were quantified using the L_3 edge because it exhibits edge-onset and multiplet peak structure that is indicative of oxidation state. The observed edge onset of each of these standard spectra are consistent with literature data, e.g., Garvie et al. (1994), Van Aken et al. (1998), Zega et al. (2003). The best-fit spectrum, $\mathbf{d}^{\mathbf{fit}}$, can then be written as the linear combination of the spectra of these three endmembers:

$$\mathbf{d}^{\mathrm{fit}} = f_{\mathrm{Fe}^0}\mathbf{d}_{\mathrm{Fe}^0} + f_{\mathrm{Fe}^{2+}}\mathbf{d}_{\mathrm{Fe}^{2+}} + f_{\mathrm{Fe}^{3+}}\mathbf{d}_{\mathrm{Fe}^{3+}} \quad (3)$$

where f_{Fe^0}, $f_{\mathrm{Fe}^{2+}}$, $f_{\mathrm{Fe}^{3+}}$, are the relative weights of each endmember spectra, and $\mathbf{d}_{\mathrm{Fe}^0}$, $\mathbf{d}_{\mathrm{Fe}^{2+}}$, $\mathbf{d}_{\mathrm{Fe}^{3+}}$ are the endmember spectra (each n × 1 vectors, where n is the number of data points in each spectrum). These best-fit weights can be determined from weighted damped least squares (e.g., Menke 2012). Fe-oxidation-state ratios are determined from normalizing the best-fit weights:

$$\%\mathrm{Fe}^0 = \frac{f_{\mathrm{Fe}^0}}{(f_{\mathrm{Fe}^0} + f_{\mathrm{Fe}^{2+}} + f_{\mathrm{Fe}^{3+}})} * 100\% \quad (4)$$

and similarly for Fe^{2+} and Fe^{3+}. Goodness of fit is evaluated using the coefficient of determination, R^2, where values of R closer to 1 imply better fits to the observed spectrum. Spectra with an R^2 value of >0.9 were accepted as having a reasonable fit (over 80% of the measured spectra) and are reported on here.

Electron-beam induced damage can alter the oxidation state of Fe-bearing materials. For example, Garvie et al. (2004) showed that Fe in cronstedtite can oxidize during EELS analysis and so care must be taken to acquire spectra free of damage effects. Thus, the potential for beam damage to affect the oxidation state of the npFe was considered during this investigation. Beam damage effects can be observed physically and/or chemically. Physical damage can manifest in the form of amorphization or, in extreme cases, the sputtering of material in the measured area. In comparison, chemical damage can take the form of oxidation or reduction. The nature of the damage depends on the material and the experimental conditions. As a general approach to our measurements, we minimized probe dwell times so as to limit electron-beam/sample interaction. Further,

we looked for qualitative real-time changes in the EELS spectra, i.e., shifting of the edge onset and/or changes in the fine structure that would suggest oxidation or reduction in the Fe. Initially, we observed both physical and chemical damage effects when using the full probe current and a long dwell time. Such effects prompted a systematic lowering of the probe current and dwell times until neither physical nor chemical damage was observed. The same collection parameters were used in the analysis of each lunar soil sample. If changes in oxidation state ratios resulted from electron beam damage, we would expect to see the resulting oxidation/reduction trend in *all* of the measurements, which we do not observe.

To evaluate the effect of oxidized Fe on the spectral properties of lunar soil, we simulated reflectance spectra with inclusions of npFe in different oxidation states. We developed a reflectance model based on the theory described in Hapke (2001, 2012). We simulated the bidirectional reflectance spectrum of a lunar regolith by modeling a mixture of pulverized rock and glass from lunar rock sample 10022 after Hapke (2001), to which increasing amounts of npFe in different oxidation states (Fe^0, Fe^{2+}, or Fe^{3+}) were added. We modeled the soil as a particulate surface in which the particles are assumed to be isotropic scatterers, and the opposition effect is ignored (Hapke 2001). Our model spectra cover visible (VIS) and near infrared (IR) wavelengths relevant for observing space weathering effects (i.e., 0.25–1.8 μm) and for interpretation of remote observations, including those from the Lunar Reconnaissance Orbiter (LRO) Wide Angle Camera (LROC/WAC; 0.41–0.69 μm), and the Moon Mineralogy Mapper (M^3) on Chandrayaan-1 (0.42–3.0 μm) (Robinson et al. 2010; Green et al. 2011).

In order to simulate the spectral reflectance of the weathered regolith we follow the procedure explained in section 8 of Hapke (2001). We begin by calculating the absorption coefficient of an unweathered host soil (α_h) from the linear addition of the individual absorption coefficients of the pulverized rock and glass from sample 10022. These were calculated from the measured reflectances of each component, using the inverted reflectance equations (13)–(23) of Hapke (2001), and assuming equal proportions of rock and glass. We then add the absorption coefficient of the npFe inclusions to find the weathered absorption coefficient: $\alpha_w = \alpha_h + \alpha_{Fe}$, where α_{Fe} is a volume-weighted linear addition of the absorption coefficients of each Fe oxidation state. To model the inclusion of oxidized states of Fe, we used the complex refractive indices of FeO and Fe_2O_3 as proxies for Fe^{2+}, and Fe^{3+}, respectively. The individual absorption coefficients of the iron phases were calculated from equations (11) and (12) of Hapke (2001), in which the values of the real and imaginary parts of the refractive indices were taken from Johnson and Christy (1974) for Fe, Henning et al. (1995) for FeO, and Tanaka (1979) and Triaud (2015) for Fe_2O_3. As in Hapke (2001), the reflectance spectra of our model weathered soil was compared to that of the weathered mare soil of sample 10084. We also modeled mixtures of oxidation states that represent the average compositions of nanoparticles measured from the immature (99% Fe^0, 0.4% Fe^{2+}, 0.6% Fe^{3+}), submature (83% Fe^0, 16% Fe^{2+}, 1% Fe^{3+}), and mature (14% Fe^0, 71% Fe^{2+}, 15% Fe^{3+}) soils and simulated their addition to the unweathered spectrum.

RESULTS

EELS Measurements

EELS spectra were collected as line profiles for over 30 nanoparticles from each sample, e.g., Fig. 1. The nanoparticles found in immature sample 12033 often appear more euhedral in shape than those in mature sample 79221. EELS spectra of nanoparticles containing Fe^0, Fe^{2+}, or Fe^{3+} have distinct $L_{2,3}$ edge onsets and structures. Fe^0 spectra have the lowest energy onset (702.0 eV), with a ~1.5 eV chemical shift between each of the subsequent onsets of Fe^{2+} (703.5 eV) and Fe^{3+} (705.0 eV). Nanoparticles that contain primarily one oxidation state exhibit EELS spectra with a single peak structure (Fig. 2a). Nanoparticles composed of two oxidation states, e.g., Fe^0 and Fe^{2+} or Fe^{2+} and Fe^{3+}, exhibit two-peaked L_3 edges (cf. Figs. 2b and 2c) with a shape intermediate between their two oxidation-state components (Garvie et al. 1994; Van Aken et al. 1999; Zega et al. 2003). The majority of particles analyzed here have a two-peak structure, with contributions only from two standard endmembers. While we did not observe three-peaked spectra, a small proportion of the nanoparticles are best modeled with contributions from each oxidation state (i.e., Fe^0, Fe^{2+}, and Fe^{3+}). The changes in the relative heights of the two-peaked L_3 edge qualitatively reflect changes in the ratio of particular Fe oxidation states to total Fe, defined herein as Fe^0 to total Fe ($Fe^0/\Sigma Fe$), Fe^{2+} to total Fe ($Fe^{2+}/\Sigma Fe$), and Fe^{3+} to total Fe ($Fe^{3+}/\Sigma Fe$). Fe-valence ratios were calculated for each spectrum using the flux-weighted, linear, least-squares method described above. Typical uncertainties in mixing ratios are 1 to 3%. The uncertainties were evaluated in a Monte-Carlo fashion, where we repeated each least squares fit several hundred times with random noise injected into each standard and sample. The random noise added to each spectrum was normally distributed with a standard deviation equivalent to the standard deviation in each observed spectrum shortward

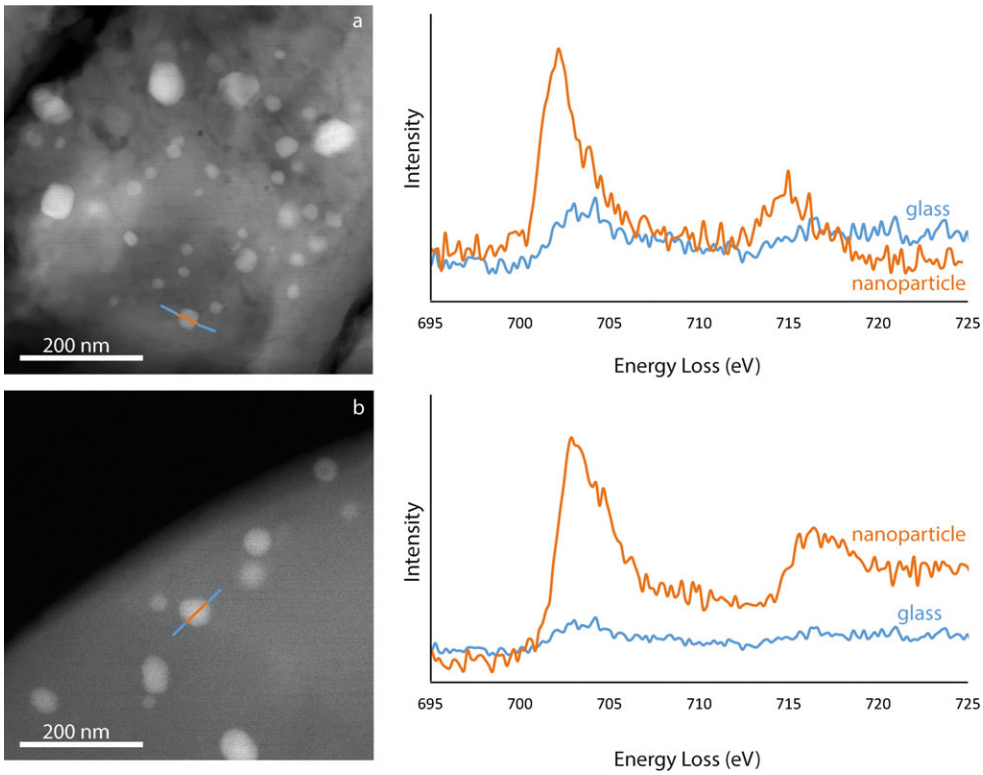

Fig. 1. STEM imaging and EELS spectra for nanoparticles in both mature and immature samples. a) STEM-HAADF image of a nanoparticle in immature soil 12033 (left panel). EELS line profile across agglutinate glass (blue) and a nanoparticle (orange), right panel. The magnitude of the Fe peak in the EELS spectrum extracted from both the glassy matrix and the nanoparticle itself is shown. b) STEM-HAADF image of a nanoparticle in mature soil 79221. NpFe in immature soils are euhedral, whereas those in more mature soils appear more spherical (left panel). EELS line profile across agglutinate glass (blue) and a nanoparticle (orange), right panel.

and longward of the L_2 and L_3 peaks. Variances in the spectra beyond these peaks likely represent random instrumental noise. The final mixing ratio uncertainty was taken as the standard deviation of the resulting suite of Monte-Carlo fits. An example best-fit spectrum for a particle from each lunar sample is shown in Fig. 2.

The quantified valence ratios for the various soil maturities are shown in ternary space (Fig. 3). Spectra collected from immature soil sample 12033 are composed mostly of Fe^0, with 84% of particles composed of 100% Fe^0. The remaining 16% of particles contain between 88 and 98% Fe^0 and residual amounts of Fe^{2+} and Fe^{3+}. The nanoparticles from the submature soil 15071 have Fe^0 compositions ranging between 38 and 100% with the remaining Fe in each particle primarily composed of Fe^{2+}. A selection of the nanoparticles measured in submature soil 15071 contain an oxidized shell surrounding a reduced core (discussed below). In comparison, spectra collected from nanoparticles in mature sample 79221 have the greatest variety of Fe oxidation states, with Fe^0 and Fe^{2+} compositions each ranging from 0 to 100%, and Fe^{3+} ranging from 0 to 56%, although the fraction of nanoparticles with such a high Fe^{3+} content is low ($\leq$15% of the total nanoparticle have Fe^{3+} >25%). The EELS results show a trend of increasing nanoparticle oxidation with increasing soil maturity; nanoparticles in immature soil (12033) are composed primarily of Fe^0, whereas those in the submature soil (15071) are a mixture of Fe^0 and Fe^{2+}, and nanoparticles in the mature soil (79221) are a mixture of Fe^{2+} and Fe^{3+}.

We note that these results should be considered in the context of measurement statistics. Due to sample thickness requirements for the EELS measurements, grains that were adequately thin and contain a high density of large Fe nanoparticles were often chosen for analysis. These grains may be among the most mature in the soil, and could contain a relatively larger fraction of oxidized Fe. Overcounting of such particles could introduce a sampling bias that is not representative of the average soil. These results do not preclude the presence of Fe^0 nanoparticles in mature soils. Our results indicate that 40% of nanoparticles in mature soil 79221 contain *no* Fe^{3+}, and >15% of those mature nanoparticles measured here contain >80% Fe^0. These findings simply indicate there is oxidized Fe present in the nanoparticles of mature lunar soils, but it is not the most abundant Fe component.

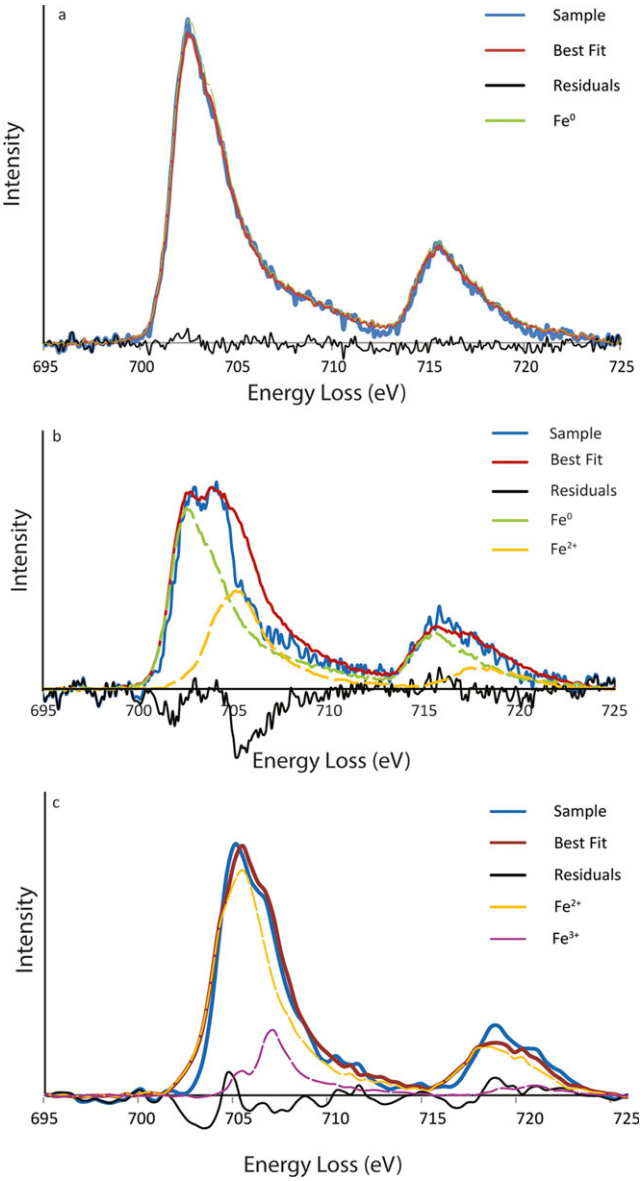

Fig. 2. Quantified EELS spectra of nanoparticles. a) Immature lunar soil sample 12033. The measured sample (blue), the best fit (red), the fit residuals (black), and the components fitting the spectrum, in this case Fe^0 (green) are shown. This particle is composed of 100% Fe^0. b) Submature lunar soil sample 15071. Colors for spectra are the same as in (a) except we have included the Fe^{2+} (gold) component. This particle is composed of 67% Fe^0 and 33% Fe^{2+}. c) Mature lunar soil sample 79221. Colors for spectra are the same as in (b) except we have included Fe^{3+} (purple) components. This particle is composed of 45% Fe^{2+} and 55% Fe^{3+}.

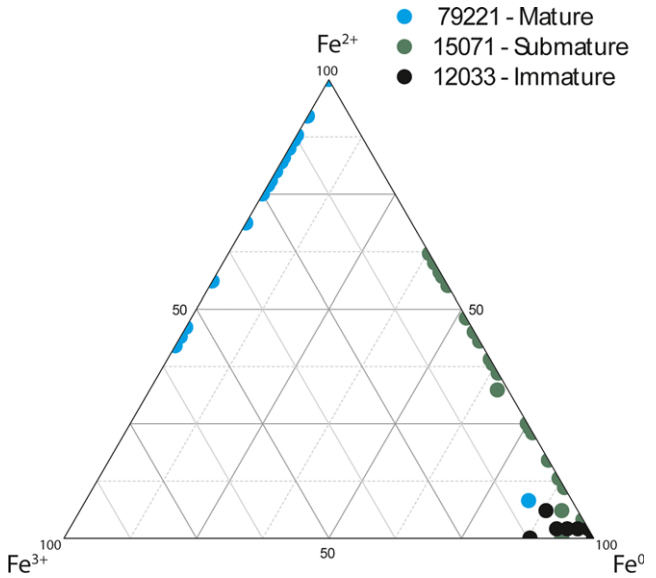

Fig. 3. Ternary plot showing compositions of nanoparticles in each of the lunar soil samples.

Particles with Oxidized Rims

A subset of particles in the submature soil (sample 15071) contain oxidized Fe in their outer edges. Quantification of EELS line profiles show that the outer three nm (on average) of these particles is composed primarily of Fe^{2+}, whereas the interior material is composed predominantly of Fe^0 (Fig. 4). This reduced-core/oxidized-shell structure was found in over 10 npFe particles that were measured in agglutinitic glass grains. This structure was only observed in nanoparticles in the submature soil, indicating it is not the result of a measurement or spectral processing artifact.

Hollow NpFe Particles

We collected STEM BF and DF images of npFe particles in each lunar soil sample. Ten nanoparticles in sample 79221 contain dark cores surrounded by bright-contrast shells (Fig. 5), suggesting that they contain a central void. As npFe is typically smaller in diameter than the thickness of the ultramicrotomed thin section, nanoparticles containing central voids may not be recognized unless the section surface happens to transect the nanoparticle core, e.g., Fig. 5. These types of nanoparticles may be in higher abundance than recognized here or in previous studies.

High-Resolution STEM Imaging

We performed STEM imaging of npFe particles in each of the three lunar soils to obtain high-resolution images of their structures. We measured interplanar *d*-spacings in one or two directions, as the data allowed, for each particle from these images (Figs. 6a–c). Measurements of npFe particles from immature sample 12033 give *d*-spacings consistent with Fe metal (Fig. 6a,

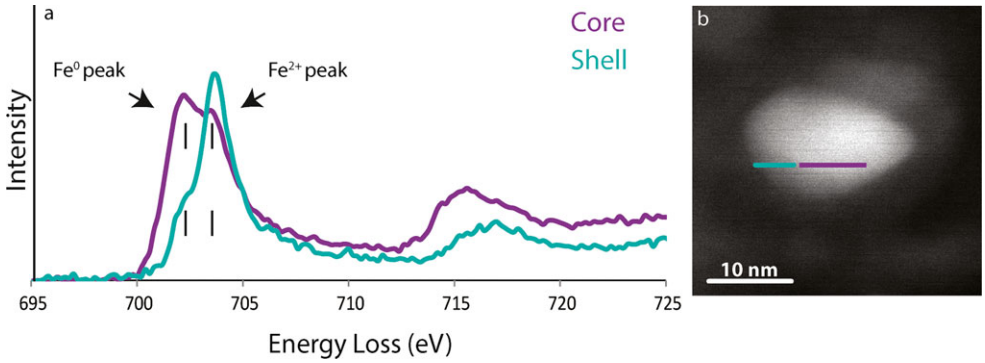

Fig. 4. TEM data for a core-shell particle. a) EELS spectra for the shell and core of the nanoparticle shown in the HAADF image (b). The shell of the nanoparticle gives a two-peaked spectrum, containing 16% Fe^0 and 84% Fe^{2+}. The core contains 79% Fe^0 and 21% Fe^{2+}.

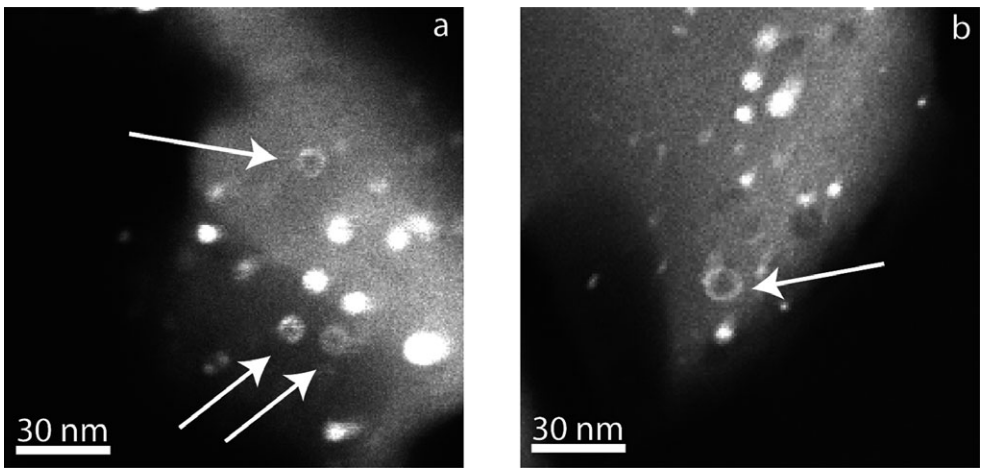

Fig. 5. DF STEM images of hollow Fe nanoparticles in mature soil sample 79221, indicated by white arrows.

Table 1). Measurements of *d*-spacings from submature sample 15071 are consistent with FeO, i.e., wüstite containing Fe^{2+} (Fig. 6b, Table 1). In comparison, the measured *d*-spacings for mature sample 79221 overlap with those of several Fe-oxide minerals (Fig. 6c, Table 1), i.e., wüstite, magnetite, and hematite, indicating possible Fe^{2+} and Fe^{3+} oxidation states. These structural measurements are consistent with the Fe oxidation states measured through EELS for each of the lunar samples.

Spectral Modeling

The results of our spectral reflectance models indicate significant differences in the behavior of certain spectral characteristics of space-weathered soils due to the Fe oxidation states in npFe (Fig. 7). Including only Fe^0 in the nanoparticles causes attenuation of the 1.0 μm absorption band, and creates a significantly darkened spectrum overall, when compared with the unweathered components (Fig. 7a). An oxidation state of Fe^{2+} in the npFe reduces the reddening effect of weathering through the mid wavelengths (0.5–1.5 μm), although the attenuation of absorption bands is similar to the addition of Fe^0 (Fig. 7a). An oxidation state of Fe^{3+} in the npFe increases the reddening effect at wavelengths >0.5 μm. In addition, the magnitude of the attenuation at the 1.0 μm silicate absorption band is slightly reduced in Fe^{3+} when compared with Fe^{2+} or Fe^0. Most noticeably, however, the simulated spectrum is significantly redder and brighter with Fe^{3+} inclusions compared to that with Fe^{2+} or Fe^0 (Fig. 7a).

We also simulated mixtures of Fe oxidation states that are representative of the compositions from each of the lunar soils, as measured using EELS (Fig. 7b). The results for the immature and submature soils are virtually indistinguishable from one another and are very similar to the measured weathered soil spectrum, although slightly reddened. The mature soil, with the highest proportion of Fe^{3+}, is brighter than the submature and immature samples.

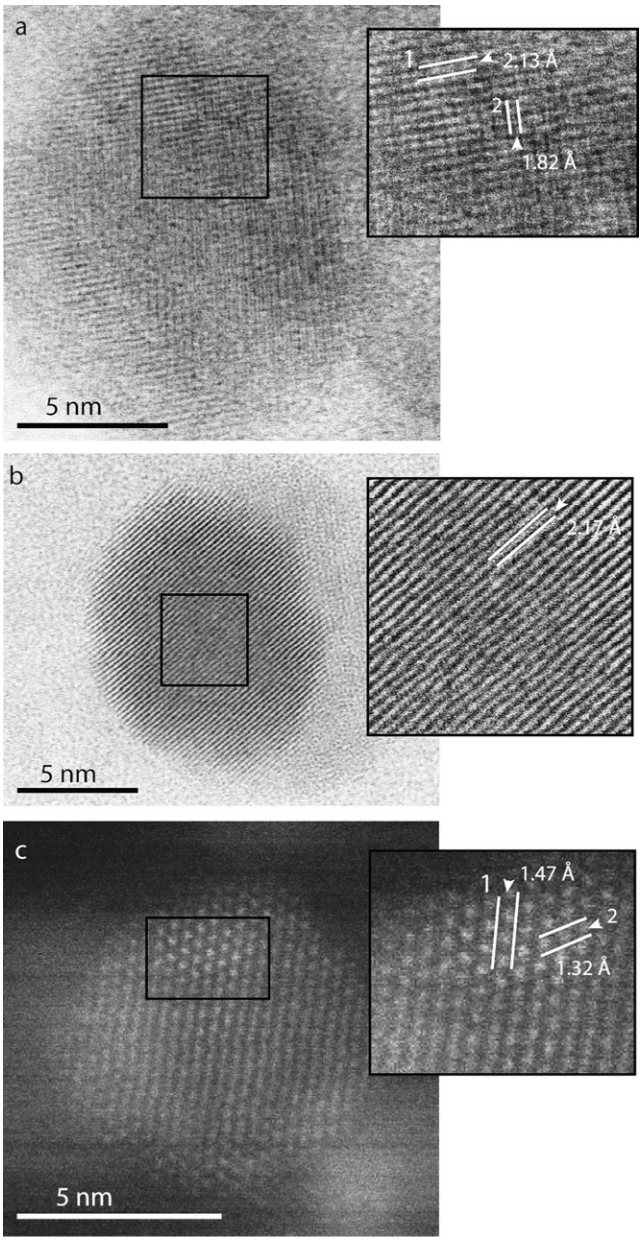

Fig. 6. High-resolution STEM images of nanoparticles in lunar soils. a) BF STEM image of nanoparticles in immature soil sample 12033. The measured *d*-spacings are consistent with Fe^0. b) BF STEM images of submature soil sample 15071. The measured *d*-spacings are consistent with FeO (wüstite). c) HAADF STEM image of a nanoparticle in mature lunar soils sample 79221. The measured *d*-spacings are consistent with Fe_3O_4 (magnetite).

Table 1. Measured *d*-spacings for npFe in lunar soil.

Sample	Measured *d*-spacings (Å)	Possible matching phase	*d*-spacing for matching phase (Å)	Miller index
12033—Immature	2.13	Fe metal	2.11	(111)
		Wüstite	2.16	(200)
	1.82	Fe metal	1.82	(200)
15071—Submature	2.17	Wüstite	2.16	(200)
79221—Mature	1.47	Magnetite	1.48	(404)
	1.32	Magnetite	1.32	(026)
			1.28	(353)
		Wüstite	1.29	(113)
		Fe metal	1.29	(220)

DISCUSSION

Crystal Chemistry and Structure

The EELS measurements show that there is a trend of increasing Fe oxidation state in nanoparticles with increasing soil maturity. The most mature soils have significant exposure times on the lunar surface and as such have experienced prolonged weathering processes. These data suggest that increased weathering time leads to increased oxidation of npFe. Several mechanisms have been proposed to describe the development of npFe particles through space weathering.

One process, which was a long-standing paradigm in lunar sample science, proposes that hydrogen (H^+) is implanted into surface soils by solar-wind irradiation and functions as a reducing agent (Hapke 2001). When these H-bearing soil grains experience melting and/or vaporization as a result of a subsequent micrometeorite impact, oxide molecules, including FeO, are liberated from the crystal structure of the grain. The implanted hydrogen acts to reduce the Fe in the melt or vapor, via the reaction:

$$FeO_{(s/l)} + 2H \rightarrow Fe_{(s)} + H_2O_{(l)}. \quad (5)$$

This pathway is expected to produce metallic Fe in lunar surface grains, and has been invoked to explain nanoparticles in agglutinate grains, which are interpreted to be melt products e.g., Housley et al. (1973). However, Fe nanoparticles also occur in amorphous rims of plagioclase grains, which have no native Fe that could otherwise be reduced, and so reaction (3) is unable to explain all observed npFe in lunar soils. Moreover, several laboratory experiments that simulate solar-wind irradiation with only He ions have demonstrated the development of Fe nanoparticles, without any implanted hydrogen, e.g., Loeffler et al. (2009). These results suggest that while nanoparticle production via reaction (3) may be occurring on the lunar surface, it cannot be the sole process by which Fe particles are produced.

Another mechanism, first proposed by Hapke et al. (1975), involves ion-irradiation of surface grains

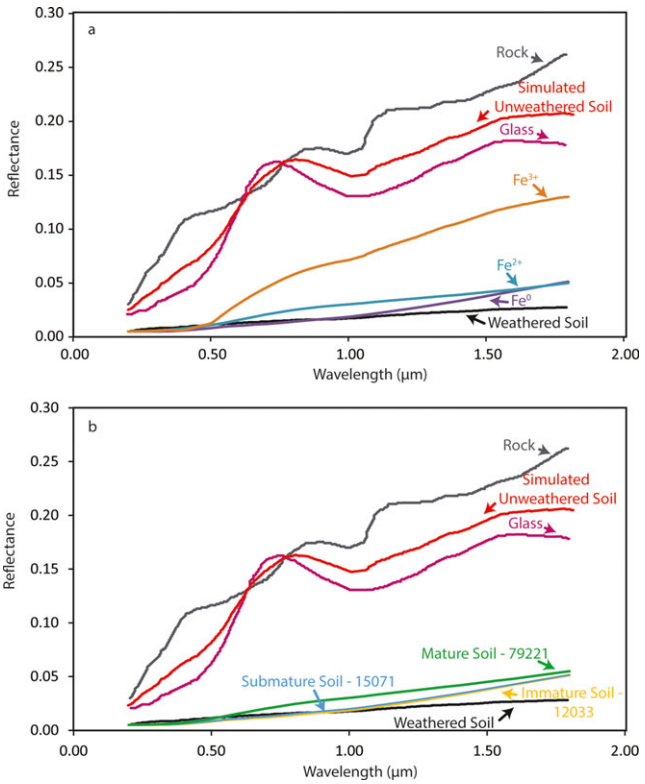

Fig. 7. Simulated reflectance spectra of lunar soil. a) Simulated unweathered soil spectrum (red) from rock (gray) and glass (magenta) components and oxidation state endmembers spectra for nanophase Fe inclusions, with Fe^0 (purple), Fe^{2+} (blue), and Fe^{3+} (orange). A measured weathered soil spectrum is shown (black) for reference. b) Unweathered components shown as in (a). Mixtures of Fe oxidation states with proportions measured from lunar soils, the immature with 99% Fe^0, 0.4% Fe^{2+}, and 0.6% Fe^{3+} (gold); submature with 83% Fe^0, 16% Fe^{2+}, and 1% Fe^{3+} (blue); and mature with 14% Fe^0, 71% Fe^{2+}, and 15% Fe^{3+} (green). A measured weathered soil spectrum in shown (black) for reference.

resulting in sputtered and redeposited material onto adjacent grains. This theory gathered support with the discovery of vapor-deposited rims in lunar soils (Keller and McKay 1993, 1997). In this ion-irradiation scenario, if O atoms are preferentially sputtered, a localized reducing environment is created on the surface of the particle, which can cause the Fe in the residual material to become reduced. The sputtered O has a low sticking coefficient, does not readily adhere to any adjacent surfaces, and is subsequently lost from the system. In contrast, as cations from the target are sputtered and redeposited onto an adjacent surface, a localized reducing environment is created on the target substrate, causing the reduction in redeposited Fe to the metallic state and the formation of nanoparticles.

A related mechanism has also been proposed for micrometeorite impacts. Oxide molecules are vaporized in the target material during an impact event, e.g., SiO, MgO, and FeO. In this vapor cloud, FeO molecules have the lowest binding energy (Hapke 2001) and consequently dissociate, resulting in independent Fe and O atoms. O, being the more volatile species, will prefer to stay in the vapor, whereas Fe will condense as nanoparticles in the surrounding glassy matrix. This formation scenario is problematic for nanoparticles in lunar agglutinates as these grains are associated with a melting process and not vapor deposition, e.g., Papike et al. (1982).

The data presented herein do not preclude any of these processes. The npFe could have been formed through a combination of these processes occurring on the surface of the Moon and other airless bodies. These processes, however, are not static. The EELS data show that the npFe in the mature soils have an oxidized Fe component, whereas those particles in the immature soils contain abundant reduced Fe. Therefore, the products of space weathering, such as npFe particles, are continually evolving after their initial formation. Mature soils have significant exposure times on the lunar surface and as such are subjected to the most prolonged weathering processes. The nanoparticles in these soils have experienced both microchemical and microstructural changes over their long lifetimes on the Moon's surface. The more spherical nature of nanoparticles in mature soils, compared to the euhedral appearance of those in the immature soil, suggest a history of microchemical processing.

There have been prior identifications of Fe^{3+} in lunar soils using techniques including RAMAN and Mössbauer spectroscopy, magnetic susceptibility, electron spin resonance studies, and electron microprobe (e.g., Ramdohr and El Goresey 1970; Weeks et al. 1970; Kolopus et al. 1971; Runcorn et al. 1971; Griscom and Marquardt 1972; Weeks 1972; Forester 1973; Bell et al. 1974; Dąbrowski et al. 2008; Pasieczna-Patkowska et al. 2008; Dikov et al. 2009; Yakovlev et al. 2009; Shearer et al., 2014). These results are often met with skepticism as the analyses of Fe^{3+}-bearing phases were not confirmed through multiple analytical techniques. In addition, some of these results were shown to have been caused by oxidation in the terrestrial atmosphere (Griscom 1974; Housley et al. 1974). However, a recent study by Joy et al. (2015) shows, using multiple analytical techniques, that the Fe^{3+}-bearing phase magnetite occurs in lunar samples. Joy et al. (2015) suggest that magnetite formed through the desulfurization of troilite in the presence of an oxidizing agent such as H_2O or CO_2. These oxidizers may be sourced from low-temperature volcanic gases, impact

vapor plumes, or impact-driven degassing of volatile-bearing regoliths.

Insight into the pathway of oxidation for npFe is provided by observations of nanoparticles in submature soil 15071. This sample is intermediary between metallic npFe in immature samples and oxidized npFe in mature samples, and their compositional differences correlate with changes in the nanoparticles' structure over time. NpFe in immature samples exhibit structures consistent with metallic Fe (bcc and fcc). Submature nanoparticles have structures matching to Fe and Fe oxide minerals, e.g., FeO (wüstite). Mature samples have nanoparticles structures matching a variety of Fe-oxide minerals, e.g., FeO, Fe_3O_4 (Fig. 6). We explore the source of this O below.

In the formation mechanisms described above, O previously bonded to Fe, is being lost from the system, with the residual O remaining in the matrix. The most abundant source of O is therefore the glassy matrix that surrounds the npFe, and we hypothesize that it is the oxidizing source of the npFe. Oxidation is nearly complete in the case of the mature sample, whereas the immature sample is composed of primarily Fe^0 nanoparticles, suggesting oxidation has not yet had time to significantly affect these samples. Fe nanoparticles may initially form in the metallic Fe state in reducing environments through one or several of the mechanisms described above. Subsequent oxidation of npFe in lunar soils could have occurred through one of several diffusion mechanisms described below.

Understanding the oxidation of Fe nanoparticles is an active field of research in the materials-science community. Fe nanoparticles, similar to those found in lunar soils, are used in a variety of biomedical and environmental applications. Due to their large surface area-to-volume ratio, Fe metal nanoparticles are highly reactive and especially prone to rapid oxidation (Bødker et al. 1994; Roy et al. 1996). Experimental work has shown that thin, oxidized films can form on Fe and other metal surfaces in only minutes when in the presence of O, even at extremely low temperatures, e.g., <100 K (Cabrera and Mott 1949). Oxidized films have also formed on surfaces of Fe metal nanoparticles that are coated in other substrates, e.g., Au, where O is hypothesized to diffuse through grain boundaries in the Au coating to oxidize the metallic core, despite no direct exposure of the metal to atmosphere (Cho et al. 2005). Such nanoparticle oxidation can proceed rapidly, forming a thin oxidized film on metallic surfaces up to ~2.0 nm in thickness in minutes (Cabrera and Mott 1949; Cabot et al. 2007). The initial growth rate of oxide layers may slow substantially but will proceed up to ~10 nm in total thickness (Cabot et al. 2007).

In synthetic nanoparticles, O initially adsorbs to and oxidizes the surface layer of the nanoparticle. The electrostatic potential difference of this adsorbed O drives electron transport from the metallic Fe core to the O on the recently formed surface oxide layer (Cabrera and Mott 1949; Cabot et al. 2007). This electron transport occurs through quantum tunneling (up to an oxide layer ~3 nm in thickness) at lower temperatures (<423 K), or through thermoemission of electrons from the Fe core into the oxide conduction band at higher temperatures (>423 K). Oxygen on the surface of the nanoparticle creates an electric field capable of driving ion diffusion (Cabrera and Mott 1949; Cabot et al. 2007), and so oxidation continues through the outward diffusion of Fe from the metallic core, through the oxide layer, to the surface of the nanoparticle where it interacts with the adsorbed O. This diffusion process leaves vacancies in the core of the nanoparticle that coalesce into a central void (Cabot et al. 2007).

In the context of space weathering, airless bodies such as the Moon lack an O-containing atmosphere, and so the npFe acquires O from the surrounding soil over time. We hypothesize that a solid-state diffusion gradient exists between the npFe and the agglutinate matrix, resulting from lack of charge neutrality, and/or unsatisfied bonds in the nanoparticle as a result of fast quenching times on the lunar surface. The diffusion rate of O to the nanoparticle surface may accelerate intermittently during episodes of nearby heating events, e.g., micrometeorite impacts. The timescales for oxidation of npFe grains are likely significantly longer than those proposed for synthetic nanoparticles, given the extreme differences in oxygen fugacity experienced by lunar soil grains and those produced in laboratories on Earth. It is possible that the npFe particles in the immature lunar soil, composed primarily of Fe^0, may have already experienced a rapid, small degree of oxidation on the surface of the Moon, evidenced by the minor oxidized Fe component of these nanoparticles.

Oxidized shells on nanoparticles, formed through diffusion mechanisms described above, were shown to be capable of developing long-range order (Bødker et al. 1994; Cabot et al. 2007). After prolonged oxidizing conditions, a hollow core may develop in nanoparticles (Cabot et al. 2007). As shown here, hollow nanoparticles occur in mature lunar soil sample 79221 (Fig. 5). This observation lends credence to the hypothesis that Fe is diffusing outward to the surface in contact with the O-containing glass. Such diffusion produces vacancies in the core of the particle leading to breakdown of long-range order and the creation of voids. We note that voids have also been reported in the cores of Fe and Fe-sulfide particles in GEMS grains

(Matsuno et al. 2015), which may have formed through similar processes.

The glass matrix in which the Fe nanoparticles occur contains Fe in the Fe^0 and Fe^{2+} valence states (Keller and Clemett 2001). Diffusion of O from the surrounding silicate glass to the nanoparticle can oxidize metallic Fe to Fe^{2+}, in the form of FeO, as discussed above. However, this oxidation process may not be adequate in producing the Fe^{3+} observed in some nanoparticles because, if it were, abundant Fe^{3+} should also be observed in the surrounding glass matrix from which the O is derived, which has not been reported. We explore below additional mechanisms for oxidizing ferrous to ferric iron.

In one such mechanism, we can consider the oxidation of Fe^{2+} to Fe^{3+} in the presence of hydrogen implanted into lunar soils by the solar wind. This hydrogen can bond with oxygen to produce water molecules that are shown to be concentrated in lunar agglutinitic glasses (Liu et al. 2012). High-resolution images of Fe nanoparticles collected from each of the soil samples indicate that the oxidized Fe in the submature and mature soils is present in the form of Fe-oxide minerals, not simply as Fe ions. Thus, a possible alternative pathway toward forming Fe^{3+} is through an Fe-oxide nanoparticle reaction with water that is concentrated in the glass matrix. The oxidation of Fe^{2+} in wüstite can produce Fe^{3+} in magnetite via:

$$3.17Fe_{0.947}O_{(s)} + 0.83H_2O_{(s)} \rightarrow Fe_3O_4(s) + 0.83H_2(gas). \quad (6)$$

This is a plausible reaction that may occur in lunar soils as this work identified FeO and Fe_3O_4 phases within the nanoparticles, and H_2O and H are known to be components of lunar soils and agglutinitic glasses (Liu et al. 2012).

If this reaction were occurring at equilibrium it would be possible to constrain an equilibrium constant for the reaction that would be dependent upon the activity of H_2O and the fugacity of H_2:

$$k_{eq} = \frac{a_{Fe_3O_4} {f_{H_2}}^{0.83}}{{a_{FeO}}^{3.17} {a_{H_2O}}^{0.83}} \quad (7)$$

where a is the activity of the solid and f is the fugacity of the gas. Assuming the Fe_3O_4 and FeO components are pure substances with activities of 1, the equilibrium constant becomes dependent upon the H_2 fugacity and the H_2O activity.

However, constraining the conditions of reaction 6, and by extension equation 7, is challenging. This reaction could be driven by episodic heating events, e.g., from an adjacent micrometeorite impact. In this case, the oxidation reaction is likely kinetic in nature, and equilibrium predictions are inapplicable. Furthermore, the thermodynamic properties of agglutinitic glasses, in which such oxidation is occurring, remain unknown. Specifically, the H_2 and H_2O components are present in the matrix (Liu et al. 2012), suggesting that the thermodynamic activity of these molecules associated with their chemical siting is important, though unknown. As a result it is not possible at this time to provide an accurately quantified temperature constraint for the proposed reaction. Future efforts at quantitatively treating this problem may require detailed experimental work, theoretical modeling, or some combination of these.

Reflectance Modeling

Varying the Fe oxidation state of lunar soils significantly alters their optical properties and modeled reflectance spectra. In particular, the addition of Fe^{3+} into npFe compositions in proportions that we measured through EELS causes noticeable reddening and brightening of the reflectance spectra. The slope of the modeled soil containing Fe^{3+} is over 50% higher (redder) than the measured soil. Thus, the degree of absorption-band attenuation and the effects that npFe particles have on the reflectance spectra of weathered materials should be reevaluated. Based on our measurements and model results, it is not appropriate to simulate space weathering effects on the Moon using pure Fe^0 nanoparticles. A variety of oxidation states, with proportions relevant to the maturity of the sample, should be considered in order to preclude under and/or over estimating the npFe concentration generating weathering characteristics. This is in contrast with recent analyses of samples from near-Earth asteroid (25143) Itokawa. Solar-flare track identification and analysis suggest that this asteroid's surface may be very immature compared to the lunar surface (Keller and Berger 2014). Thus, for some asteroids it may be more appropriate to create reflectance models of asteroidal surfaces with a singular Fe oxidation state, Fe^0.

Understanding the effects that different Fe oxidation states have on the characteristics of reflectance spectra could contribute to a deeper understanding of the distribution of soil maturities from remote sensing data on airless bodies such as the Moon. Analyzing the reflectance spectra for different regions of the Moon and comparing them to simulated spectra with reduced and oxidized Fe nanoparticle contributions may allow us to determine remotely the relative maturities of sample regions. This insight could contribute to our understanding of regolith processing

and landscape evolution on the surface of the Moon and other airless bodies.

CONCLUSIONS

EELS measurements of nanophase Fe in space-weathered lunar soils of varying maturities show that the Fe in the nanoparticles occurs in Fe^0, Fe^{2+}, and Fe^{3+} oxidation states. The EELS measurements are corroborated through phase identification via high-resolution imaging. Immature soils primarily contain reduced, metallic Fe^0 nanoparticles; submature soils contain Fe^0 and Fe^{2+}; and mature soils contain Fe^{2+} and Fe^{3+}. In the submature sample we found npFe with oxidized shells. We hypothesize that the oxidation of npFe is a result of the diffusion of O atoms through the surrounding glassy matrix to the nanoparticle surface over time. We show that there is a significant difference in the modeled reflective properties of lunar soil when including npFe particles with a range of oxidation states. Future efforts to simulate space weathering may need to consider oxidized Fe when modeling the spectral reflectance of the surface of an airless body. A spectral model that more accurately accounts for the microscale chemical complexity of the surface could be used to understand the macroscale chemical and physical evolution of airless body landscapes from remote sensing data.

Acknowledgments—We thank CAPTEM for allocation of lunar samples for this study. We gratefully acknowledge the use of facilities within the Leroy Eyring Center for Solid State Science at Arizona State University, with assistance from Dr. Toshihiro Aoki. We thank Lindsay Keller and Larry Taylor for their reviews, and Carle Pieters for editorial guidance, which improved this manuscript. We thank Dante Lauretta for providing helpful advice on the manuscript. We also acknowledge the use of Electron Beam Analysis Labs at the NASA Johnson Space Center. Funding for M.S. Thompson is provided by the Natural Sciences and Engineering Research Council of Canada (NSERC) and the NASA Earth and Space Science Fellowship (NESSF). Research supported in part by NASA.

Editorial Handling—Dr. Carle Pieters

REFERENCES

Bell P., Mao H., and El Goresy A. 1974. A study of iron-rich particles on the surfaces of orange glass spheres from 74220. Proceedings, 4th Lunar and Planetary Science Conference. pp. 187–191.

Bødker F., Mørup S., and Linderoth S. 1994. Surface effects in metallic iron nanoparticles. *Physical Review Letters* 72:282.

Cabot A., Puntes V. F., Shevchenko E., Yin Y., Balcells L., Marcus M. A., Hughes S. M., and Alivisatos A. P. 2007. Vacancy coalescence during oxidation of iron nanoparticles. *Journal of the American Chemical Society* 129:10,358–10,360.

Cabrera N. and Mott N. 1949. Theory of the oxidation of metals. *Reports on Progress in Physics* 12:163.

Cho S.-J., Idrobo J.-C., Olamit J., Liu K., Browning N. D., and Kauzlarich S. M. 2005. Growth mechanisms and oxidation resistance of gold-coated iron nanoparticles. *Chemistry of Materials* 17:3181–3186.

Dąbrowski A., Mendyk E., Robens E., Skrzypiec K., Goworek J., Iwan M., and Rzączyńska Z. 2008. Investigation of surface properties of lunar regolith part III. *Journal of Thermal Analysis and Calorimetry* 94:633–639.

Dikov Y. P., Gerasimov M., Yakovlev O., and Ivanov A. 2009. Valence state of iron in a condensate from the Luna 16 regolith. *Petrology* 17:429–438.

Egerton R. 1996. *Electron energy loss in the electron microscope*, vol. 160. New York: Plenum. pp. 165–169.

Forester D. 1973. Mössbauer search for ferric oxide phases in lunar materials and simulated lunar materials. Proceedings, 3rd Lunar and Planetary Science Conference. p. 2697.

Garvie L. A. and Buseck P. R. 1998. Ratios of ferrous to ferric iron from nanometre-sized areas in minerals. *Nature* 396:667–670.

Garvie L. A., Craven A. J., and Brydson R. 1994. Use of electron-energy loss near-edge fine structure in the study of minerals. *American Mineralogist* 79:411–425.

Garvie L. A., Zega T. J., Rez P., and Buseck P. R. 2004. Nanometer-scale measurements of $Fe^{3+}/\Sigma Fe$ by electron energy-loss spectroscopy: A cautionary note. *American Mineralogist* 89:1610–1616.

Green R. O., Pieters C., Mouroulis P., Eastwood M., Boardman J., Glavich T., Isaacson P., Annadurai M., Besse S., Barr D., Buratti B., Cate D., Chatterjee A., Clark R., Cheek L., Combe J., Dhingra D., Essandoh V., Geier S., Goswami J. N., Green R., Haemmerle V., Head J., Hovland L., Hyman S., Klima R., Koch T., Kramer G., Kumar A. S. K., Lee K., Lundeen S., Malaret E., McCord T., McLaughlin S., Mustard J., Nettles J., Petro N., Plourde K., Racho C., Rodriquez J., Runyon C., Sellar G., Smith C., Sobel H., Staid M., Sunshine J., Taylor L., Thaisen K., Tompkins S., Tseng H., Vane G., Varanasi P., White M., and Wilson D. 2011. The Moon Mineralogy Mapper (M^3) imaging spectrometer for lunar science: Instrument description, calibration, on-orbit measurements, science data calibration and on-orbit validation. *Journal of Geophysical Research: Planets* 116: E00G19.

Griscom D. 1974. Ferromagnetic resonance spectra of lunar fines: Some implications of line shape analysis. *Geochimica et Cosmochimica Acta* 38:1509–1519.

Griscom D. and Marquardt C. 1972. Evidence of lunar surface oxidation processes: Electron spin resonance spectra of lunar materials and simulated lunar materials. Proceedings, Lunar and Planetary Science Conference. p. 2397.

Hapke B. 2001. Space weathering from Mercury to the asteroid belt. *Journal of Geophysical Research: Planets* 106:10,039–10,073.

Hapke B. 2012. *Theory of reflectance and emittance spectroscopy*, 2nd ed. New York: Cambridge University Press.

Hapke B., Cassidy W., and Wells E. 1975. Effects of vapor-phase deposition processes on the optical, chemical, and magnetic properties of the lunar regolith. *The Moon* 13:339–353.

Henning T., Begemann B., Mutschke H., and Dorschner J. 1995. Optical properties of oxide dust grains. *Astronomy and Astrophysics Supplement Series* 112:143.

Housley R., Grant R., and Paton N. 1973. Origin and characteristics of excess Fe metal in lunar glass welded aggregates. Proceedings, Lunar and Planetary Science Conference. p. 2737.

Housley R., Cirlin E., Paton N., and Goldberg I. 1974. Solar wind and micrometeorite alteration of the lunar regolith. Proceedings, 5th Lunar and Planetary Science Conference. pp. 2623–2642.

Johnson P. and Christy R. 1974. Optical constants of transition metals: Ti, V, Cr, Mn, Fe Co, Ni, and Pd. *Physical Review B* 9:5056.

Joy K. H., Visscher C., Zolensky M. E., Mikouchi T., Hagiya K., Ohsumi K., and Kring D. A. 2015. Identification of magnetite in lunar regolith breccia 60016: Evidence for oxidized conditions at the lunar surface. *Meteoritics & Planetary Science* 50:1157–1172.

Keller L. P. and Berger E. L. 2014. A transmission electron microscope study of Itokawa regolith grains. *Earth, Planets and Space* 66:1–7.

Keller L. P. and Clemett S. J. 2001. Formation of nanophase iron in the lunar regolith (abstract #2097). Lunar and Planetary Science Conference. CD-ROM.

Keller L. P. and McKay D. S. 1993. Discovery of vapor deposits in the lunar regolith. *Science* 261:1305–1307.

Keller L. P. and McKay D. S. 1997. The nature and origin of rims on lunar soil grains. *Geochimica et Cosmochimica Acta* 61:2331–2341.

Keller L. P., Wentworth S., and McKay D. S. 1998. Space weathering: Reflectance spectroscopy and TEM analysis of individual lunar soil grains (abstract #1762). 29th Lunar and Planetary Science Conference. CD-ROM.

Kolopus J., Kline D., Chatelain A., and Weeks R. 1971. Magnetic resonance properties of lunar samples: Mostly Apollo 12. Proceedings, Lunar and Planetary Science Conference. p. 2501.

Krivanek O. L., Dellby N., Murfitt M. F., Chisholm M. F., Pennycook T. J., Suenaga K., and Nicolosi V. 2010. Gentle STEM: ADF imaging and EELS at low primary energies. *Ultramicroscopy* 110:935–945.

Liu Y., Guan Y., Zhang Y., Rossman G. R., Eiler J. M., and Taylor L. A. 2012. Direct measurement of hydroxyl in the lunar regolith and the origin of lunar surface water. *Nature Geoscience* 5:779–782.

Loeffler M., Dukes C., and Baragiola R. 2009. Irradiation of olivine by 4 keV He^+: Simulation of space weathering by the solar wind. *Journal of Geophysical Research: Planets* 114:E03003.

Matsuno J., Miyake A., Tsuchiyama A., Messenger S., and Nakamura-Messenger K. 2015. Complete TEM-tomography: 3D structure of GEMS cluster (abstract #2177). 46th Lunar and Planetary Science Conference. CD-ROM.

Menke W. 2012. *Geophysical data analysis: Discrete inverse theory*. Boston: Academic Press.

Morris R. 1978. The surface exposure/maturity/of lunar soils—Some concepts and Is/FeO compilation. Proceedings, 9th Lunar and Planetary Science Conference. pp. 2287–2297.

Muller D., Kourkoutis L. F., Murfitt M., Song J., Hwang H., Silcox J., Dellby N., and Krivanek O. 2008. Atomic-scale chemical imaging of composition and bonding by aberration-corrected microscopy. *Science* 319:1073–1076.

Noble S. K., Pieters C. M., and Keller L. P. 2007. An experimental approach to understanding the optical effects of space weathering. *Icarus* 192:629–642.

Papike J., Simon S., White C., and Laul J. 1982. The relationship of the lunar regolith less than 10 micrometer fraction and agglutinates. I—A model for agglutinate formation and some indirect supportive evidence. Proceedings, 12th Lunar and Planetary Science Conference. pp. 409–420.

Pasieczna-Patkowska S., Dąbrowski A., Robens E., and Ryczkowski J. 2008. FT-IR/PAS studies of lunar regolith samples. *Acta Physica Polonica A. Optical and Acoustical Methods in Science and Technology* 114:A163–A168.

Pieters C. M., Taylor L. A., Noble S. K., Keller L. P., Hapke B., Morris R. V., Allen C. C., McKay D. S., and Wentworth S. 2000. Space weathering on airless bodies: Resolving a mystery with lunar samples. *Meteoritics & Planetary Science* 35:1101–1107.

Ramdohr P. and El Goresey A. 1970. Opaque minerals of the lunar rocks and dust from Mare Tranquillitatis. *Science* 167:615–618.

Robinson M. S., Brylow S. M., Tschimmel D., Humm D., Lawrence S. J., Thomas P. C., Denevi B. W., Bowman-Cisneros E., Zerr J., Ravine M. A., Caplinger M. A., Ghaemi F. T., Schaffner J. A., Malin M. C., Mahanti P., Bartels A., Anderson J., Tran T. N., Eliason E. M., McEwen A. S., Turtle E., Jolliff B. L., and Hiesinger H. 2010. Lunar reconnaissance orbiter camera (LROC) instrument overview. *Space Science Reviews* 150:81–124.

Roy S., Roy B., and Chakravorty D. 1996. Magnetic properties of iron nanoparticles grown in a glass matrix. *Journal of Applied Physics* 79:1642–1645.

Runcorn S., Collinson D., O'Reilly W., Stephenson A., Battey M., Manson A., and Readman P. 1971. Magnetic properties of Apollo 12 lunar samples. *Proceedings of the Royal Society* 3258:157–174.

Sasaki S., Nakamura K., Hamabe Y., Kurahashi E., and Hiroi T. 2001. Production of iron nanoparticles by laser irradiation in a simulation of lunar-like space weathering. *Nature* 410:555–557.

Shearer C., Sharp Z., Burger P., McCubbin F., Provencio P., Brearley A., and Steele A. 2014. Chlorine distribution and its isotopic composition in "rusty rock" 66095. Implications for volatile element enrichments of "rusty rock" and lunar soils, origin of "rusty" alteration, and volatile element behavior on the Moon. *Geochimica et Cosmochimica Acta* 139:411–433.

Tanaka T. 1979. Optical constants of polycrystalline 3d transition metal oxides in the wavelength region 350 to 1200 nm. *Japanese Journal of Applied Physics* 18:1043.

Triaud A. H. M. J. Database of optical constants for cosmic dust. http://www.astro.unijena.de/Laboratory/OCDB/oxsul.html. Accessed: April 27, 2015.

Van Aken P., Liebscher B., and Styrsa V. 1998. Quantitative determination of iron oxidation states in minerals using Fe

$L_{2,3}$-edge electron energy-loss near-edge structure spectroscopy. *Physics and Chemistry of Minerals* 25:323–327.

Van Aken P., Styrsa V., Liebscher B., Woodland A., and Redhammer G. 1999. Microanalysis of $Fe^{3+}/\Sigma Fe$ in oxide and silicate minerals by investigation of electron energy-loss near-edge structures (ELNES) at the Fe $M_{2,3}$ edge. *Physics and Chemistry of Minerals* 26:584–590.

Varela M., Oxley M., Luo W., Tao J., Watanabe M., Lupini A. R., Pantelides S., and Pennycook S. 2009. Atomic-resolution imaging of oxidation states in manganites. *Physical Review B* 79:085117.

Weeks R. 1972. Magnetic phases in lunar material and their electron magnetic resonance spectra: Apollo 14. Proceedings, Lunar and Planetary Science Conference. pp. 2503.

Weeks R., Kolopus J., Kline D., and Chatelain A. 1970. Apollo 11 lunar material: Nuclear magnetic resonance of 27Al and electron resonance of Fe and Mn. *Geochimica et Cosmochimica Acta Supplement* 1:2467.

Williams D. and Carter C. 1996. *Transmission electron microscopy: A textbook for material science*. New York: Springer.

Yakovlev O., Dikov Y. P., and Gerasimov M. 2009. Effect of the disproportionation reaction of ferrous iron in impact-evaporation processes. *Geochemistry International* 47:134–142.

Zega T. J., Garvie L. A., and Buseck P. R. 2003. Nanometer-scale measurements of iron oxidation states of cronstedtite from primitive meteorites. *American Mineralogist* 88:1169–1172.